Microscopy and Microanalysis (2019), 1–7
doi:10.1017/S1431927619000667

Microscopy AND Microanalysis

Original Article

Effect of Heavy Mass Ion (Gold) and Light Mass Ion (Boron) Irradiation on Microstructure of Tungsten

Prashant Sharma[1]*, Padivattathumana Maya[1], Satyaprasad Akkireddy[2], Prakash M. Raole[1], Anil K. Tyagi[1,3], Asha Attri[1], Pawan K. Kulriya[4], Parmendra K. Bajpai[5], Sudhir Mishra[6], Shiv P. Patel[5], Tarkeshwar Trivedi[5], K. B. Khan[6] and Shishir P. Deshpande[1,3]

[1]ITER-India, Institute for Plasma Research, Bhat, Gandhinagar 382428, India; [2]Institute for Plasma Research, Bhat, Gandhinagar 382428, India; [3]Homi Bhabha National Institute, Training School Complex, Anushaktinagar, Mumbai 400094, India; [4]Inter-University Accelerator Centre Aruna Asaf Ali Marg, New Delhi 110067, India; [5]Guru Ghasidas Vishwavidyalaya, Koni, Bilaspur 495009, India and [6]Bhabha Atomic Research Centre, Mumbai 400 085, India

Abstract

The difference in the defect structures produced by different ion masses in a tungsten lattice is investigated using 80 MeV Au^{7+} ions and 10 MeV B^{3+} ions. The details of the defects produced by ions in recrystallized tungsten foil samples are studied using transmission electron microscopy. Dislocations of type $\boldsymbol{b} = 1/2[111]$ and [001] were observed in the analysis. While highly energetic gold ion produced small clusters of defects with very few dislocation lines, boron has produced large and sparse clusters with numerous dislocation lines. The difference in the defect structures could be due to the difference in separation between primary knock-on atoms produced by gold and boron ions.

Key words: dislocation loop, electron microscopy, irradiation-induced defects, PKA spectrum, tungsten

(Received 1 November 2018; revised 7 February 2019; accepted 5 May 2019)

Introduction

In a nuclear fusion reactor, a hot and dense hydrogen isotope-plasma interacts with the materials that are surrounding it and depositing a high MW/m^2 (up to 20 MW/m^2) heat into them (Pitts et al., 2013; Federici et al., 2017). The plasma-facing materials, therefore, need to have a high melting point. The energetic hydrogen isotopes also cause the erosion of the wall materials and in addition they become trapped in the wall (Roth et al., 2009). From a reactor view point therefore, the plasma-facing material should have low erosion yield and very little ability of H-isotope trapping. The latter aspect results in stringent operational constraints in the form of radioactivity of tritium ($^3_1$H). Tungsten has emerged as one of the most promising candidates for plasma-facing materials because of its high melting point (3,695 K), low erosion yield, and low hydrogen affinity (Kaufmann & Neu, 2007; Lassner & Schubert, 2012). However, while exposed to the products of nuclear fusion reactions, 14.1 MeV neutrons, and 3.5 MeV α-particles, tungsten is going to accumulate radiation damage. The defects produced due to irradiation can enhance the T-trapping, which may adversely affect the operational lifetime of the reactor from the nuclear regulatory view point (Taylor et al., 2017). Therefore, there is an urgent need to estimate the H-isotope trapping in the defects created by neutrons. At present, there exists no high energy, high fluence fusion-relevant neutron source. Therefore, ion irradiation is carried out in tungsten to mimic the displacement damage created by a neutron. While neutrons dissipate their energy mainly in elastic collisions and nonelastic nuclear collisions, ions in the lattice slow down by inelastic collisions with electrons as well as elastic collisions. The maximum kinetic energy of a recoiled tungsten atom created by neutrons is about 300 keV. The damage rate created by neutrons is about 10^{-7} dpa/s, and to study a reactor relevant dpa (1–10 dpa), the experiments need to be carried out for several years. Ions, on the other hand, have the advantage that, depending on the ion current and mass, very high dpa levels can be achieved in short time (~hours) without causing transmutation of the materials (Was, 2007).

Heavy ion and self-ion implantation experiments have been carried out by various authors to study the effect of dpa in the damage and defect microstructure (Hideo et al., 2014; Ogorodnikova et al., 2014; Oya et al., 2015). They have shown that ion irradiation primarily results in vacancy and interstitial clustering at room temperature. Dislocation lines and prismatic dislocation loops are also been reported by various authors (Grzonka et al., 2014; Hasanzadeh et al., 2018). Irradiation due to low mass gaseous ions on the other hand has shown the formation of vacancy clusters (Labelle, 2011). All the above experiments differed in their mass, fluence, energy, and the implantation range and consequently the rate of creation of damage and the total dpa were also different. The formation of the defect structure is a complex process which involves the contribution of all the above parameters along with the irradiation temperature. In this paper, we systematically investigate the effect of ion mass on the damage creation by choosing two extrema of mass. We

***Author for correspondence:** Prashant Sharma, E-mail: prashanttopquark@gmail.com, prashant.sharma@iter-india.org

Cite this article: Sharma P *et al* (2019) Effect of Heavy Mass Ion (Gold) and Light Mass Ion (Boron) Irradiation on Microstructure of Tungsten. *Microsc Microanal.* doi:10.1017/S1431927619000667

present the results of damage from heavy gold ions (197 amu) of 80 MeV energy and 10 MeV boron ions (11 amu). The energy of ions is so chosen that their penetration range overlaps (~4.5 μm). The ion flux was kept constant in both the experiments such that the effect of ion mass can be elucidated.

Experimental

Mechanically polished cold-rolled tungsten foils of 8 mm × 8 mm × 0.1 mm size were annealed in vacuum at 10^{-3} mbar with a 100 mbar Ar + 8% H_2 gas environment at 1,838 K for about an hour. The annealing temperature chosen was above the recrystallization threshold of tungsten (~1,473 K). The samples were irradiated with 80 MeV Au^{7+} ions for a fluence of 1.3×10^{14} ions/cm^2 using a 15 MV van de Graff generator (Pelletron), at IUAC Delhi (Kanjilal et al., 1993). The beam current was 1–1.5 nA (flux ~1×10^{10} ions/cm^2/s) and the total irradiation time was 3 h. This amounts to a total dpa of 0.22 by using the Kinchin–Pease damage model in the SRIM software with a displacement energy of 90 eV, surface energy of 2 eV, and lattice energy of 3 eV (Kinchin & Pease, 1955; Ziegler et al., 2010). The dpa values are calculated by taking into account the entire damage depth calculated by SRIM. At such high implantation energies, surface sputtering is not expected. The rate of dpa was 2×10^{-5}/s. Another set of samples were irradiated with 10 MeV B^{3+} ions for the same fluence (flux ~8.7×10^{10} ions/cm^2/s) by using the tandem accelerator facility at GGU Bilaspur (Trivedi et al., 2017). The total dpa obtained was about 0.001 and the rate of dpa was 5×10^{-7}/s. The range of both the ions was about 4.5 μm and the average energy lost in the electronic system for Au was about 65 and 9.5 MeV for B. The ion range and dpa values are given in Figure 8. All the irradiation experiments have been carried out at room temperature.

Transmission electron microscopy (TEM) analysis has been carried out in recrystallized foil, Au-irradiated, and B-irradiated foil. For comparison, TEM investigations have also been carried out in the pristine foil before recrystallization. The specimen preparation and TEM investigations have been carried out in an FEI (300 keV) Tecani G2 F30 S-TWIN at FCIPT-IPR, Gandhinagar, India. The samples for TEM are 3 mm in diameter with a thickness of typically ~200 nm or less. This thickness was reduced to the required level in various sequential thinning and polishing steps. A sample of 3 mm in disc form was punched out from a 100 μm-thick foil of the dimension of 8 mm × 8 mm using a Gatan disc punch (model 659). The 3 mm disc was ground, using a Gatan disc grinder (model 623), on a fine lapping sheet of 5 μm-sized abrasive particles and the thickness of the disc was brought down to 80 μm. This ground disc was subjected to pre-thinning and polishing using a Gatan dimple grinder (model 656). In this process, a phosphor bronze wheel, along with diamond paste and alumina suspension, was used for achieving the necessary pre-thinning and polishing of the disc sample. After this process, the thickness of the sample was reduced to 20 μm at its central area while at the rim the thickness was still maintained at 80 μm. This is required to facilitate the handling of the sample. After this dimple grinding, the sample was subjected to ion milling using a Gatan PIPS-II. In this process, two ion guns are used for polishing the sample by sputtering material from its surface. Argon ions with an energy of 5 keV were used. After the completion of the milling, the thickness of a small region of the sample at its middle was reduced to <200 nm which was electron transparent.

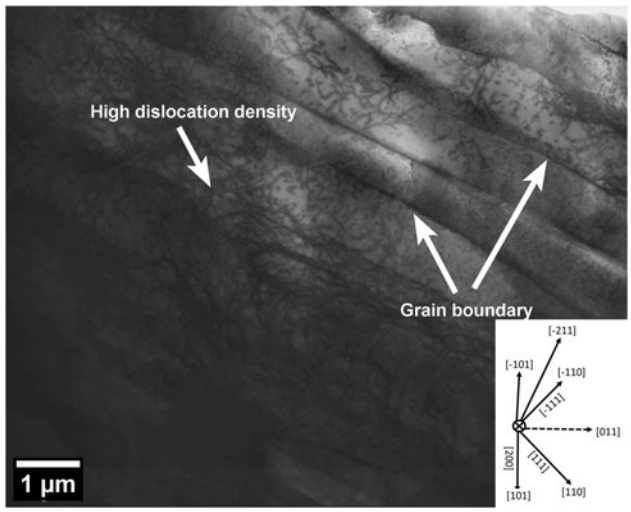

Fig. 1. Transmission electron micrograph of pristine tungsten foil.

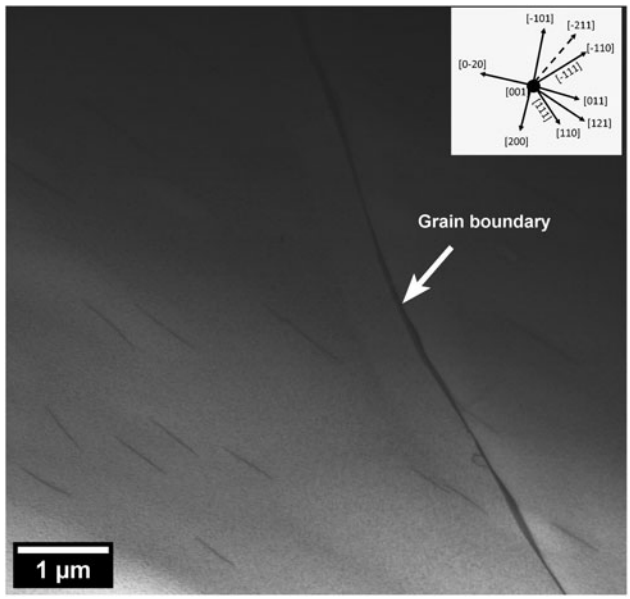

Fig. 2. Transmission electron micrograph of annealed tungsten foil.

Results and Discussion

The microstructure of the pristine, recrystallized, and irradiated samples was analyzed using TEM. The dislocation analysis of the samples was carried out using ImageJ software (Rueden et al., 2017). The dislocation density of the samples was quantified by analyzing the TEM images using the line-intercept method (Norfleet et al., 2008). In this method, three lines of length (L) 10 μm were drawn along random directions on the image. The dislocation density (ρ) is calculated by taking the ratio of the number of intersection points of these lines with the dislocations, N, to the product of line length (L) and average sample thickness (t) [$\rho = (N/Lt)$. An average thickness of 200 nm was considered in the calculations.

Figure 1 shows the transmission electron micrograph of the pristine tungsten foil. The pristine foil consists of elongated grains due to cold-rolling. The elongation of grains is observed in [121]

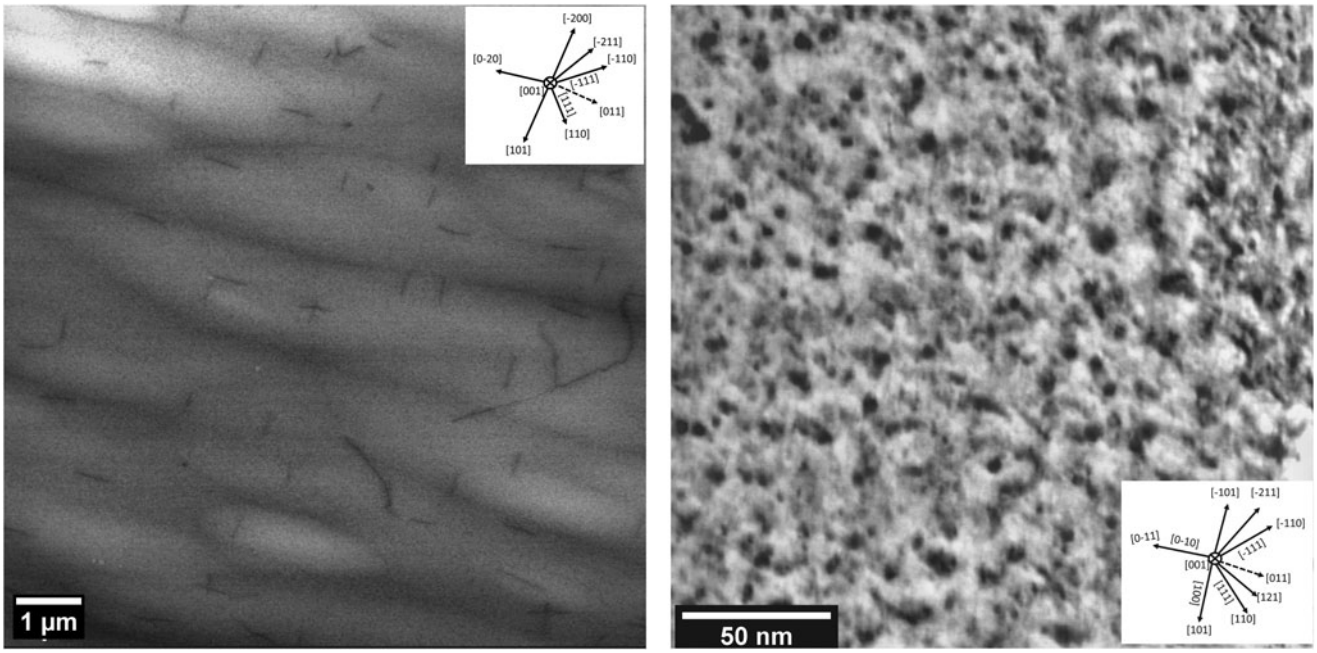

Fig. 3. a: Transmission electron micrograph at 2 μm depth of tungsten foil after 80 MeV Au-irradiation for 0.22 dpa (fluence 1.3×10^{14} ions/cm^2), (**b**) high magnification view of the same image.

crystallographic direction which indicates the direction of rolling of the foil. A high dislocation density (>2.3×10^{10}/cm^2) is observed along the grain boundaries and within the grains. The high dislocation density zones were attributed to the plastic flow due to heavy deformation during the rolling. The average grain size of the pristine samples was found to be 2 μm.

Figure 2 shows the transmission electron micrograph of the annealed (at 1,838 K) tungsten foil. From the visual examination, it can be concluded that the grain growth and recrystallization have taken place during annealing. From Figure 2 it may be noted that the microstructure shows a much reduced dislocation density in comparison to the pristine foil. This may be due to the recombination of dislocations near the grain boundary during annealing. The recrystallized W-foil contained dislocations of lengths from 300 to 1,000 nm with 5.7×10^8/cm^2 density. The crystallographic orientation of the foil is shown in the inset at the top right of the image. The bright field image, with visibility criterion ($\vec{g} \cdot \vec{b}neq0$), identified dislocations of $\boldsymbol{b}$ =1/2 [−111] and 1/2 [111] near the zone axis [001] with the diffraction vector $\boldsymbol{g}$ [−211] (dotted arrow) in the bright field image of the foil. A higher density of the dislocations is observed parallel to the [121] direction.

Figure 3a shows the TEM micrographs of (a) 80 MeV Au-irradiated tungsten foil with 1.3×10^{14} Au/cm^2 fluence corresponding to 0.22 dpa. The images were taken at a depth of 2 μm from the surface. The figure shows dislocation lines of lengths from 200 to 2,500 nm which are larger in comparison to the lines observed in the recrystallized foil (up to a maximum of 1,000 nm). The dislocation density was found to be 6.0×10^8/cm^2 which is slightly higher than what is observed in the recrystallized sample (5.7×10^8/cm^2). The bright field image of dislocations is shown with the diffraction vector $\boldsymbol{g}$ [011] (dotted arrow) near the [001] zone axis. The dislocations identified as $\boldsymbol{b} = 1/2[-111]$ and 1/2 [111] are parallel to the directions [−110] and [110]. Many of the dislocations are found parallel to the [101] directions.

Figure 3b shows the high magnification view of the same sample. Small clusters of dislocations 2–10 nm in size adjacent to each other are observed in the micrograph. The cluster density was found to be 1.6×10^{12}/cm^2. The Burgers vector analysis showed that clusters with $\boldsymbol{b} = 1/2[-111]$, 1/2 [111], [0-10], and [001] are identified in diffraction contrast with $\boldsymbol{g}$ [011] near the [001] zone axis. The clusters with [001] are observed along the direction normal to the foil plane. The clusters 1/2 [111] parallel to the direction [110] has the highest density observed in the foil.

Figure 4a shows diffraction pattern and Figure 4b shows the schematics of the crystallographic orientation of the Au-irradiated tungsten foil. The diffraction pattern was taken at the zone axis [001]. The schematic illustrates the shape of clusters parallel to the [-110], [110], [101], and [0-11] directions. Clusters of Burgers vector $\boldsymbol{b} = \langle 001 \rangle$ parallel to the [001] direction are shown as complete circles and elongated shapes parallel to other directions, and clusters with $\boldsymbol{b} = 1/2\langle 111 \rangle$were observed elongated in the [110] direction.

Figure 5a shows the electron micrographs of a 10 MeV B-irradiated W-foil at 2 μm depth for a fluence of 1.3×10^{14} ions/cm^2 corresponding to a dpa of 0.001. We have observed dislocation lines, loops, and clusters of defects in the analysis. The figure shows branched dislocation lines varied in length from 150 to 1,500 nm. The dislocation line density is found to be 1.7×10^9/cm^2. The dislocations of Burgers vector $\boldsymbol{b} = 1/2[1-11]$ and 1/2 [111] are identified for $\boldsymbol{g}$ [101] near zone axis [11-1]. Some dislocation rafts parallel to the direction [0-11] are also observed.

Figure 5b shows the high magnification view of the same sample. Defect clusters varied in size between 8 and 35 nm and are observed as the dark dots in the micrograph. The cluster density was found to be 9.3×10^9/cm^2. Dislocation loops varied in size between 25 and 70 nm were observed which is marked with an arrow. The loop density was found to be 6.8×10^8/cm^2. The dislocation loops [−100], [010], [00-1], 1/2 [11-1], 1/2 [1-11], and 1/2 [111] are identified with $\boldsymbol{g}$ [211] near zone axis [11-1].

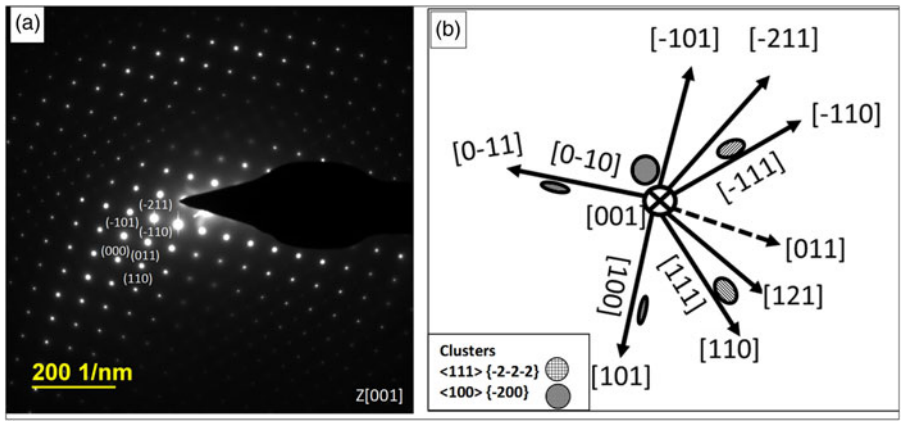

Fig. 4. Electron diffraction pattern (**a**) and schematic of the crystallographic directions of bcc tungsten (**b**) of Au-irradiated foil at zone axis [001].

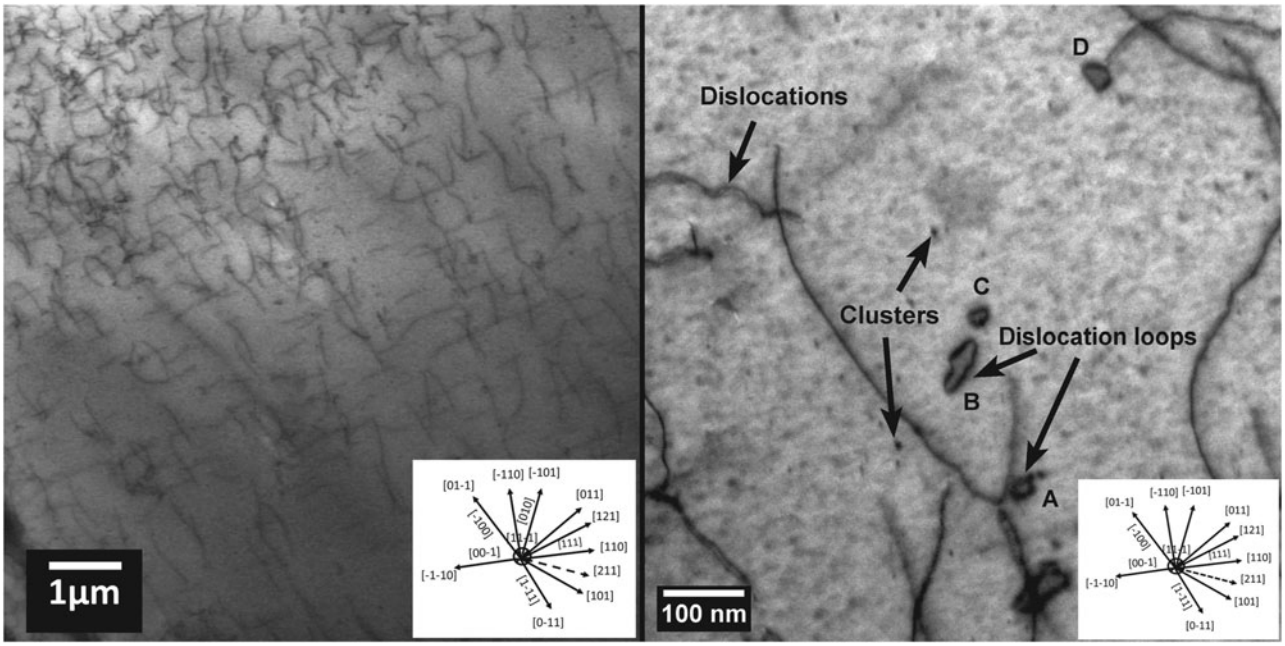

Fig. 5. a: Transmission electron micrograph at 2 μm depth of tungsten foil after 80 MeV Au-irradiation for 0.22 dpa (fluence 1.3×10^{14} ions/cm^2), (**b**) high magnification view of the same image.

In the image, loop A is circular and identified as $\boldsymbol{b} = 1/2[11-1]$. The plane of the loop A is normal to zone axis which implies a circular or rectangular shape. Dislocation loop B is identified as [010], which is elongated and parallel to the [−101] direction. Similarly, loop C is identified as 1/2 [111] and parallel to the [110] direction. Loop D is [−100] which is parallel to the direction [01-1].

Figures 6a and 6b show the diffraction pattern and the schematics of the crystallographic orientation of the B-irradiated tungsten foil. The diffraction pattern was taken near zone axis [11-1] in the B-irradiated foil. The schematic illustrates the shape of clusters parallel to the [−110], [110], [101], and [0-11] directions. Clusters with Burgers vector <001> parallel to the [001] direction are shown in a complete circle and elongated shape parallel to other direction. A summary of various defects observed and their density and size is given in Table 1.

Figures 7a and 7b show the high-resolution TEM images of the Au and B ions irradiated W-foils. Figure 7a shows defect clusters in the tungsten lattice as indicated by the arrows, after Au-irradiation. Dislocation loops observed in B-irradiated foil are shown in Figure 7b. The heavily distorted lattice planes in Figure 7a could be due to high defect cluster (vacancy and interstitial) density observed in Au-irradiated samples. Figure 7b shows dislocation and vacancy dislocation loops with the agreement of Figure 5b.

The 80 MeV Au ion irradiation led to the formation of dislocation lines and a cluster of defects in tungsten lattice. However, boron irradiation produced dislocation loops, apart from the dislocation lines and clusters. Although the irradiation fluence of both the ions was kept constant, i.e., 1.3×10^{14}/cm^2, the type of defects and their distribution was found to be different. While longer dislocation lines were observed in the case of

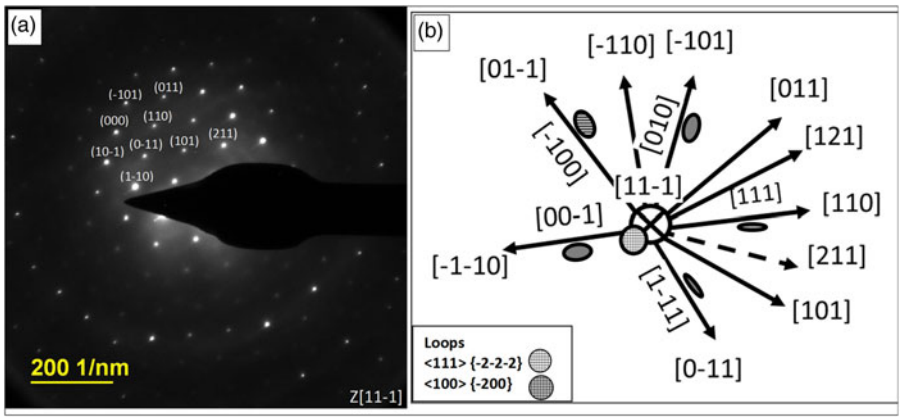

Fig. 6. Electron diffraction pattern (**a**) and schematic of the crystallographic directions of bcc tungsten (**b**) of B-irradiated foil at zone axis [11-1].

Table 1. Summary of Defects and Measurements of Their Density and Sizes.

Samples	Fluence (cm^{-2})	Dislocation Density (cm^{-2})	Average Dislocation Size Range (nm)	Loop Size (nm)	Loop Density (cm^{-2})	Cluster Size (nm)	Cluster Density (cm^{-2})
Pristine	–	$>2.3 \times 10^{10}$	–	–	–	–	–
Annealed at 1,838 K	–	5.7×10^{8}	300–1,000	–	–	–	–
80 MeV Au-irradiated tungsten foil	1.3×10^{14}	6.0×10^{8}	200–2,500	–	–	2–10	1.6×10^{12}
10 MeV B-irradiated tungsten foil	1.3×10^{14}	1.7×10^{9}	150–1,500	25–70	6.8×10^{8}	8–35	9.3×10^{9}

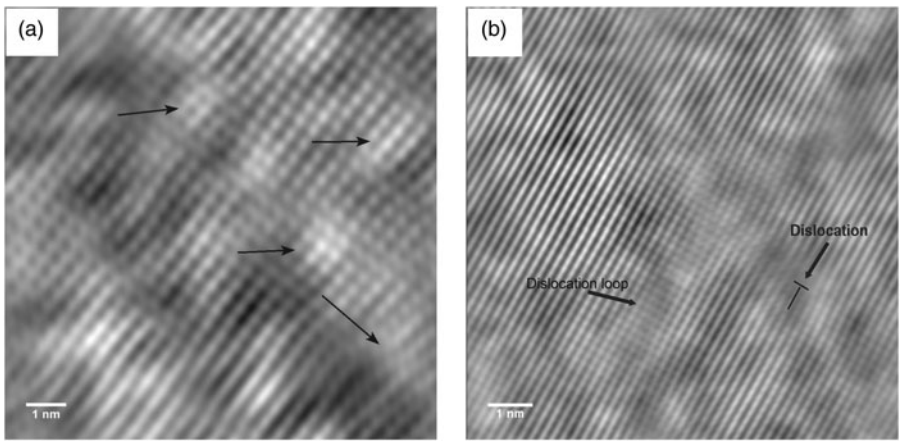

Fig. 7. High-resolution TEM images of Au-irradiated (**a**) and (**b**) B-irradiated W-foils.

Au-irradiated samples, the line density was roughly an order of magnitude higher in the case of B-irradiation. The defect clusters were found to be smaller with small inter-cluster separation in the case of Au-irradiation leading to higher cluster densities in comparison to B-irradiation. This could be due to the difference in the damage energy available for the defect formation which manifests in the differences in the primary knock-on atom (PKA) distribution in the lattice. The number of defects produced per ion due to 80 MeV Au-ions and 10 MeV B-ions was calculated from SRIM (Ziegler, 1988; Ziegler et al., 2010) and is shown in Figure 8. It can be seen that gold ions produce 1,000 times more defects at 2 μm depth in comparison to boron ions. The small inter-PKA separation of high-energy PKA in the case of gold ions leads to the spontaneous formation of small defect clusters. *In-situ* TEM observations have shown the spontaneous nucleation of defect clusters at low temperature due to high-energy PKA in tungsten (Yi et al., 2016). The larger inter-PKA separation of low-energy PKA leads to the formation of isolated Frenkel pairs. The interstitial diffusion at low temperature might have led to the formation of large-scale defects (Was & Andresen, 2014; Nandipati et al., 2015) as observed in the case of 10 MeV boron.

The gold ion-irradiated foil contains dislocations of the larger average size of ~1,300 nm compared with that of ~800 nm which were found in boron ion-irradiated foil. This might imply the

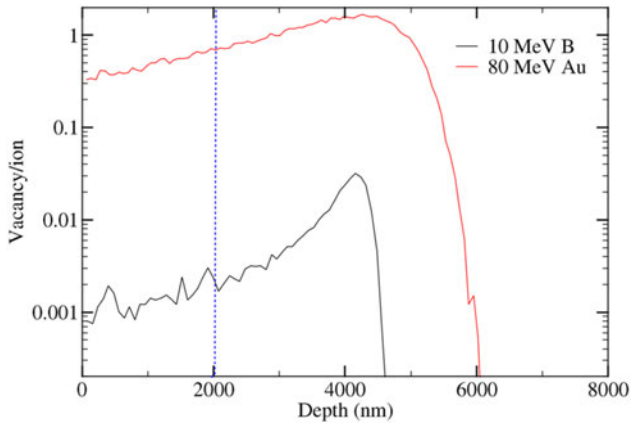

Fig. 8. Depth profile of vacancy produced per ion calculated from SRIM.

formation of large screw dislocations in the case of Au-irradiated samples. The line energy of an edge dislocation is always larger than that of a screw dislocation. For a Poisson ratio $\nu \approx 1/3$, the quantity $(1-\nu) < 1$, and the energy of the screw dislocation, $E_{screw} \approx 0.66\, E_{edge}$. This means the dynamics allows either a dislocation that tends to have as large a screw component as possible for minimization of energy by dislocation interaction or reaction or rafting/fastening of dislocations (Chou, 1972; Hull & Bacon, 2011; Yao et al., 2013). In order to minimize the energy, the dislocation needs to have a zig-zag shape as much as geometrically allowed, which enhances its screw character which is observed in the case of Au-irradiated samples. Whereas, in the B-irradiated sample, short and fastened dislocations are present in the form of a network which is of edge in character. Dislocation loop formation is governed by the defect interaction such as glide and climb of mobile defects and dislocations in the lattice.

Summary and Conclusions

In order to study the effect of ion mass in the damage creation, we have carried out irradiation experiments with two largely different mass ions of 80 MeV Au (197 amu) and 10 MeV B (11 amu). The ion fluence and range are kept the constant for both the ions, i.e., 1.3×10^{14} ions/cm^2 and ~4.5 μm. The dpa in the experiments correspond to 0.22 and 0.001 for a displacement energy of 90 eV. Transmission electron micrographs from 2 μm deep from the surface are analyzed. The major observations from the study are:

- In tungsten, gold ions produced small (2–10 nm), dense clusters of defects while boron ions produce large (8–35 nm) and sparse clusters of defects. The cluster density in Au-irradiated samples (1.6×10^{12}/cm^2) was found to be 2 orders of magnitude higher than that of B-irradiated samples (9.3×10^{9}/cm^2).
- The major Burgers vectors identified in the irradiated samples were 1/2 [−111], 1/2 [111], and 1/2 [1-11]. Long dislocation lines were observed in Au ion-irradiated foil; on the other hand, a network of dislocations was observed in B ion-irradiated samples.
- The clusters with $\boldsymbol{b}$ = [0-10], [001], 1/2 [−111], and 1/2 [111] were identified near the [001] zone axis in the irradiated samples. The high density of clusters with $\boldsymbol{b} = 1/2$ [111] was observed parallel to the [110] direction in the Au-irradiated foil. The dislocation loops with $\boldsymbol{b}$ = [−100], [010], [00-1], 1/2 [1-11], and 1/2 [111] were identified near the [11-1] zone axis in boron-irradiated foil samples.

The difference in the defect structures of Au- and B-irradiated samples might be due to the inter-PKA separation. While gold produces several high-energy PKA that can cause spontaneous nucleation of defect clusters at the end of cascade, boron produces low-energy PKA that predominantly formed isolated Frenkel pairs. The diffusion and agglomeration of them might have led to the formation of large-scale structures in the boron-irradiated samples.

Acknowledgments. Part of this work was completed under IAEA-CRP agreement number 18183/R0. Ramesh Kumar Buddu, K. Mokaria Prakash (Annealing and characterization) from IPR Gandhinagar are acknowledged.

References

Chou YT (1972). Dislocation reactions and networks in anisotropic b.c.c. crystals. *Mater. Sci. Eng. C* **100**, 81–86. doi: 10.1016/0025-5416(72)90071-7.

Federici G, Biel W, Gilbert MR, Kemp R, Taylor N & Wenninger R (2017). European DEMO design strategy and consequences for materials ITER conceptual design. *Nucl Fusion* **570**(092002), 1–25. doi: 10.1088/1741-4326/57/9/092002.

Grzonka J, Ciupiński L, Smalc-Koziorowska OV, Ogorodnikova M, Mayer KJ & Kurzydłowski (2014). Electron microscopy observations of radiation damage in irradiated and annealed tungsten. *Nucl. Instr. Meth. Phys. Res. B* **340**, 27–33. 10.1016/j.nimb.2014.07.043.

Hasanzadeh S, Schäublin R, Décamps B, Rousson V, Autissier E, Barthe MF & Hébert C (2018). Three-dimensional scanning transmission electron microscopy of dislocation loops in tungsten. *Micron* **1130**(May), 24–33. doi: 10.1016/j.micron.2018.05.010.

Hideo W, Naoki F, Shiori N & Naoaki Y (2014). Microstructure and thermal desorption of deuterium in heavy-ion-irradiated pure tungsten. *J Nucl Mater* **4550**(1–3), 51–55. doi: 10.1016/j.jnucmat.2014.03.060.

Hull D & Bacon JD (2011). *Introduction to Dislocations*, vol. **1**. 5th ed. Oxford, UK: Butterworth-Heinemann, Elsevier Ltd. 10.1016/B978-0-08-096672-4.00006-2.

Kanjilal D, Chopra S, Narayanan MM, Iyer IS, Vandana J, Joshi R & Datta SK (1993). Testing and operation of the 15UD Pelletron at NSC. *Nucl. Instr. Meth. Phys. Res. A* **3280**(1–2), 97–100. doi: 10.1016/0168-9002(93)90610-T.

Kaufmann M & Neu R (2007). Tungsten as first wall material in fusion devices. *Fusion Eng Des* **820**(5–14), 521–527. doi: 10.1016/j.fusengdes.2007.03.045.

Kinchin GH & Pease RS (1955). The displacement of atoms in solids by radiation. *Rep Prog Phys* **180**(1), 1–51. doi: 10.1088/0034-4885/18/1/301.

Labelle AJ-RR (2011). The Effects of Helium on Deuterium Retention in Tungsten Under Simultaneous Irradiation. Thesis, University of Toronto.

Lassner E & Schubert WD (2012). *Tungsten: properties, chemistry, technology of the element, alloys, and chemical compounds*. USA: Springer. ISBN 9781461549079.

Nandipati G, Setyawan W, Heinisch HL, Roche KJ, Kurtz RJ & Wirth BD (2015). Displacement cascades and defect annealing in tungsten, part III: The sensitivity of cascade annealing in tungsten to the values of kinetic parameters. *J Nucl Mater* **462**, 345–353. doi: 10.1016/j.jnucmat.2015.01.059.

Norfleet DM, Dimiduk DM, Polasik SJ, Uchic MD & Mills MJ (2008). Dislocation structures and their relationship to strength in deformed nickel microcrystals. *Acta Mater* **560**(13), 2988–3001. doi: 10.1016/j.actamat.2008.02.046.

Ogorodnikova OV, Gasparyan Y, Efimov V, Ciupinski L & Grzonka J (2014). Annealing of radiation-induced damage in tungsten under and after irradiation with 20 MeV self-ions. *J Nucl Mater* **4510**(1), 379–386. ISSN0022-3115.

Oya Y, Li X, Sato M, Yuyama K, Zhang L, Kondo S, Hinoki T, Hatano Y, Watanabe H, Yoshida N & Chikada T (2015). Thermal desorption

behavior of deuterium for 6 MeV Fe ion irradiated W with various damage concentrations. *J Nucl Mater* **461**, 336–340. doi: 10.1016/j.jnucmat.2015.03.032.

Pitts RA, Carpentier S, Escourbiac F, Hirai T, Komarov V, Lisgo S, Kukushkin AS, Loarte A, Merola M, Sashala Naik A, Mitteau R, Sugihara M, Bazylev B & Stangeby PC (2013). A full tungsten divertor for ITER: Physics issues and design status. *J Nucl Mater* **4380**(Suppl), S48–S56. doi: 10.1016/j.jnucmat.2013.01.008.

Roth J, Tsitrone E, Loarte A, Loarer T, Counsell G, Neu R, Philipps V, Brezinsek S, Lehnen M, Coad P, Grisolia C, Schmid K, Krieger K, Kallenbach A, Lipschultz B, Doerner R, Causey R, Alimov V, Shu W, Ogorodnikova O, Kirschner A, Federici G & Kukushkin A (2009). Recent analysis of key plasma wall interactions issues for ITER. *J Nucl Mater* **390–3910**(1), 1–9. doi: 10.1016/j.jnucmat.2009.01.037.

Rueden CT, Johannes S, Hiner MC, DeZonia BE, Walter AE, Arena ET & Eliceiri KW (2017). Imagej2: Imagej for the next generation of scientific image data. *BMC Bioinformatics* **180**(1), 529. doi: 10.1186/s12859-017-1934-z.

Taylor N, Merrill B, Cadwallader L, Di Pace L, El-Guebaly L, Humrickhouse P, Pinna T, Panayotov D, Reyes S, Porfiri M-T, Shimada M & Willms S (2017). Materials-related issues in the safety and licensing of nuclear fusion facilities ITER conceptual design recent citations. *Nucl Fusion* **570**(092003), 1–28.

Trivedi T, Patel Shiv P, Chandra P & Bajpai PK (2017). Ion beam facilities at the national centre for accelerator based research using a 3 MV Pelletron accelerator. *Phys Procedia* **900**(November), 100–106. doi: 10.1016/j.phpro.2017.09.032.

Was GS (2007). *Fundamentals of Radiation Materials Science*, vol. **44**. Berlin, Heidelberg, New York: Springer. ISBN 9788578110796. doi: 10.1017/CBO9781107415324.004.

Was GS & Andresen PL (2014). *Woodhead Publishing Series in Energy*. Cambridge, UK: Woodhead Publishing. pp. 355–420. 10.1533/9780857097552.2.355.

Yao B, Edwards DJ & Kurtz RJ (2013). TEM characterization of dislocation loops in irradiated bcc Fe-based steels. *J Nucl Mater* **4340**(1–3), 402–410. doi: 10.1016/j.jnucmat.2012.12.002.

Yi X, Jenkins ML, Kirk MA, Zhou Z & Roberts SG (2016). In-situ TEM studies of 150 keV W+ ion irradiated W and W-alloys: Damage production and microstructural evolution. *Acta Mater* **112**, 105–120. doi: 10.1016/j.actamat.2016.03.051.

Ziegler JF (1988). The stopping and range of ions in solids. In *Ion Implantation Science and Technology*, Ziegler JF (Ed.), 2nd ed.Ed. pp. 3–61. London, UK: Academic Press10.1016/B978-0-12-780621-1.50005-8.

Ziegler JF, Ziegler MD & Biersack JP (2010). SRIM—The stopping and range of ions in matter (2010). *Nucl. Instr. Meth. Phys. Res. B* **2680**(11–12), 1818–1823. doi: 10.1016/j.nimb.2010.02.091.